

Accepted Manuscript

A novel membrane electrode assembly design for proton exchange membrane fuel cells: Characterization and performance evaluation

Samaneh Shahgaldi, Adnan Ozden, Xianguo Li, Feridun Hamdullahpur



PII: S0013-4686(19)30077-5
DOI: 10.1016/j.electacta.2019.01.064
Reference: EA 33467
To appear in: *Electrochimica Acta*
Received Date: 24 September 2018
Accepted Date: 10 January 2019

Please cite this article as: Samaneh Shahgaldi, Adnan Ozden, Xianguo Li, Feridun Hamdullahpur, A novel membrane electrode assembly design for proton exchange membrane fuel cells: Characterization and performance evaluation, *Electrochimica Acta* (2019), doi: 10.1016/j.electacta.2019.01.064

This is a PDF file of an unedited manuscript that has been accepted for publication. As a service to our customers we are providing this early version of the manuscript. The manuscript will undergo copyediting, typesetting, and review of the resulting proof before it is published in its final form. Please note that during the production process errors may be discovered which could affect the content, and all legal disclaimers that apply to the journal pertain.

A novel membrane electrode assembly design for proton exchange membrane fuel cells: Characterization and performance evaluation

Samaneh Shahgaldi^a, Adnan Ozden^{a,b}, Xianguo Li^{a,b}, Feridun Hamdullahpur^b

^a20/20 Laboratory for Fuel Cell and Green Energy RD&D, Department of Mechanical and Mechatronics Engineering, University of Waterloo, 200 University Avenue West, Waterloo, ON N2L 3G1, Canada

^bDepartment of Mechanical and Mechatronics Engineering, University of Waterloo, 200 University Avenue West, Waterloo, ON N2L 3G1, Canada

Corresponding author: xianguo.li@uwaterloo.ca (Xianguo Li) Tel.: +1 519 888 45 67

Abstract

Conventional membrane-electrode assembly (MEA), a key component in proton exchange membrane fuel cells, only operates reasonably within a narrow range of operating conditions. In this study, a scaled-up MEA that can perform adequately under a wide range of humidification and flow conditions is developed. It consists of a microporous layer (MPL) composed of graphene for the cathode electrode, catalyst layers (CLs) prepared with a short-side-chain (SSC) ionomer, and a SSC electrolyte membrane. The results show that the graphene-based MPL employed on the cathode provides an excellent platform for the CL (hence promotes catalyst activity and catalyst utilization) and improves water retention, due to its unique microstructure and morphology. The proposed MEA provides stable and highly promising performance independent of flow conditions under the relative humidities (RHs) of 70% and 100%. Interestingly, the MEA also demonstrates relatively better cell performance under low-humidity conditions (40% RH), such that it performs noticeably better, as the reactants are supplied to the cell under low-flow condition, rather than moderate- and high-flow conditions.

Keywords: Proton exchange membrane fuel cell; Membrane electrode assembly design; Graphene-based microporous layers; Short-side-chain (SSC) ionomers and membranes

1. Introduction

Proton exchange membrane (PEM) fuel cells have received a surge of interest as a clean power generator [1–3]. Membrane electrode assembly (MEA), as the key component of the PEM fuel cells, uses conventional long-side-chain (LSC) ionomers and membranes, requiring full hydration for desirable cell performance; so that the current state-of-the-art fuel cells perform adequately only under quite a narrow range of operating conditions, such as flow and humidity of the reactants, although the use of two-layered gas diffusion layers (GDLs) with the microporous layer (MPL) provides improved water management, hence enhanced cell performance at high current density operation [4–6]. This illustrates the pressing need for innovative designs for MEAs suitable for a wide range of operating conditions [7].

The key to achieve this goal is the design of MEAs in such a way that an effective balance between water removal and water retention is established for a wide range of the operating conditions [8–10]. Such a balance could be achieved partially through the modification of the surface wettability [11], and the use of MPL, in particular on the cathode electrode [4,12]. However, due to the complexity and the conflicting requirement between reactant transport and water management, and the extent of the operation conditions required in practice, these techniques still work only for a limited range of operating conditions, and even in some instances only at a specific operating condition (see [7,13–17], for example).

Such condition-dependent optimization has been investigated in recent years. It has been shown that an effective balance between water retention and water removal for a particular loading depends on the wettability of the MPLs [7]. For example, an increase in the relative humidities (RHs) of reactant streams improves the performance of MEAs with hydrophobic MPL [18]. In contrast, MEAs composed of hydrophilic MPL suffers less from membrane dehydration under low-humidity operation, and more from water flooding under high-

humidity conditions [19]. However, unfortunately, up to now, no MPL design has completely met the performance demands over the range of operating conditions that are likely to be encountered in cell operation (i.e., low-, moderate-, and fully-humidified conditions).

A significant challenge to water balance in MEAs is the ever-changing water generation rate, due to the continuous changes in loading conditions. For example, an increase in current density triggers more water generation, and in this scenario, the extra water must be expelled from the MEA quickly; on the other hand, a decrease in current density gives rise to less water generation, and in this case, water must be retained for sufficient membrane humidification [20,21]. An ideal MEA should be designed to have the capability of tolerating instantaneous and/or continuous variations in operating conditions, so that the cell can perform adequately, independent of operating conditions [7].

The need for water balance is because the use of conventional long-side-chain (LSC) ionomers and membranes, in which ionic transport occurs adequately solely in the presence of sufficient water in the polymeric matrix [22,23]. Thus, these ionomers and membranes are quite sensitive to humidification levels, such that they cannot function properly in the presence of either excess or insufficient water [23]. In consequence, these LSC ionomers and membranes can perform quite differently, depending on the humidification levels in the cell, meaning that they are not completely suitable for fuel cell operation, in which humidification level varies substantially [24].

The objective of the present study is therefore to develop an MEA design that can perform effectively under a wide range of operating conditions (i.e., flow and humidification conditions). In the proposed MEA design, an MPL made of graphene is employed on the cathode electrode for effective water retention [25,26], a catalyst layer (CL) comprised of a short-side-chain (SSC) ionomer for its high ionic conductivity, high durability, and high water

retention capability [27–29], and a SSC membrane for its unique proton transport capability (noticeably higher ionic conductivity than the conventional long-side-chain (LSC) ionomer membranes) and excellent insensitivity to water content in the polymer matrix. The morphological, microstructural, and physical properties of the porous components of the MEA developed are characterized. Cell performance of the MEA designed is investigated in a single scaled-up fuel cell under various operating conditions. Cyclic voltammetry (CV) analyses are also performed to elucidate the catalyst activity and catalyst utilization characteristics of the MEA developed.

2. Experimental

2.1. Materials

Avcarb EP40 carbon paper (without MPL and hydrophobic agent treatment) is used as a cathode single-layer gas diffusion layer (GDL), Avcarb GDS3250 (with MPL and hydrophobic agent treatment) as a commercially available anode double-layer GDL, carbon-supported Pt (Pt/C, 40 wt% Pt to C ratio) as both anode and cathode catalysts, short-side-chain (SSC) ionomer (Aquivion[®] PFSA, with an equivalent weight of 720 g eq⁻¹) as a polymeric binder, SSC perfluorosulfonic acid ionomer membrane (Fumapem[®] FS-715-RFS) as an electrolyte membrane, isopropyl alcohol (2-propanol, IPA, 99.9%) as a solvent, and deionized (DI) water as a diluting agent. For the cathode MPL manufacturing, the materials employed include commercially available graphene powder (heXo-G V20, NanoXplore, BET surface area: 30 m²/g) used as a main building material, isopropyl alcohol (2-propanol, IPA, 99.9%) as a solvent, polytetrafluoroethylene (PTFE, 60 wt%, water-based dispersion) as a hydrophobic agent, and deionized (DI) water as a diluting agent. For porosimetry analyses, octane (>99%, anhydrous) is used as a working fluid.

2.2. Microporous layer (MPL) manufacturing

In the proposed MEA design, the double-layer GDL employed in the cathode side is made of graphene-based MPL, which is spray-deposited onto the single-layer GDL (Avcarb EP40) by following a procedure similar to [13]. The procedure basically involves three sequential stages: 1) graphene powder, isopropyl alcohol, and deionized water are consecutively put into a glass beaker, then mechanically mixed in an ultrasonic bath for 2 h under room conditions; 2) the resulting slurry is spray-deposited onto the single-layer GDL under a vacuum environment at 75°C until the graphene and hydrophobic agent loadings of 1.0 mg/cm² and 20.0 wt% are achieved, respectively; and 3) the double-layer GDL (MPL deposited on the single-layer GDL) is initially dried at 240°C for 1 h, and then sintered at 350°C for 40 min.

2.3. Membrane electrode assembly (MEA) manufacturing

First, the catalyst slurry is prepared by adding the constituent materials, Pt/C, isopropyl alcohol, and deionized (DI) water, sequentially to a glass vial and ultrasonically mixing for 1 h under room conditions; the resulting slurry is then deposited onto both surfaces of the membrane until the anode and cathode loadings of 0.10 and 0.40 mg/cm², respectively, with the Pt/C-ionomer ratio of 3.0/1.0 for both the anode and cathode electrodes. Finally, the MEA is formed by sandwiching the catalyst-coated membrane between the anode and cathode GDLs.

2.4. Morphological, microstructural and physical characterization of the anode and cathode double-layer GDLs and electrodes

The surface morphologies of the anode and cathode GDLs and CLs are investigated via an ultra-high resolution field emission scanning electron microscope (Zeiss Ultra SEM 55). For better quality of imaging, scanning electron microscopy (SEM) images are collected from the surfaces after gold deposition.

Microstructural characteristics of the double-layer GDLs are investigated via a standard porosimetry (Porotech Standard Porosimeter, 3.10) by following a well-established procedure, whose details can be found in [25,30]. However, in its basic form, the procedure relies on (i) extracting two pieces of test specimens from the test-of-interest double-layer GDLs in disk-like forms, (ii) evacuating the air from the specimens under a vacuum environment, (iii) immersing the specimens along with two standard ones in a glass vessel filled with octane, (iv) mounting the specimens between the two standard ones and allowing them to reach capillary equilibrium, (v) recording the changes in the weights of the specimens at time intervals of 3 min while they are still stacked, and eventually (vi) obtaining the capillary pressure curve of the specimens by utilizing the known capillary pressure curves of the standard ones. Upon determination of the capillary pressure curves, as the representatives of pore characteristics, the microstructural parameters, i.e., porosity, pore size distribution, mean pore size, cumulative pore volume, pore surface area, and bulk density, are determined [30].

The through-plane gas permeability is determined for the anode and cathode double-layer GDLs in a manner similar to [25,31], to provide insights into their capability of convection-governed mass transport. The measurements are conducted by following several sequential steps, including (i) extracting two pieces of disk-like specimens from the test-of-interest double-layer GDLs, (ii) mounting the specimens as a stack between two metallic plates, (iii) supplying the working fluid (air in the present case) across the sample at 75°C with various flow rates, (iv) measuring the corresponding pressure drops between the top and bottom sides of the specimens, and finally (v) calculating the through-plane gas permeability via Darcy's Law for single-phase one-dimensional (1D) compressible flow.

The surface wettability characteristics of the anode and cathode double-layer GDLs are determined via a static contact angle goniometer (Ramé-Hart Instrument) with the sessile drop technique. The measurement procedure followed includes (i) extracting three pieces of

disk-like specimens from the test-of-interest double-layer GDL, (ii) mounting each pieces on an anti-vibrating bench, (iii) dropping water droplets with a constant volume of 7 μl at different locations on the surface of each specimen using a syringe, (iv) fitting tangent lines to the points where the droplets touch the surfaces, and lastly (v) measuring the static contact angle via software. The measurements are conducted with three different specimens at at least 20 different locations on the specimens with the standard deviation of less than 2%.

2.5. Electrochemical characterization

To investigate the electrochemical characteristics of the MEAs designed and fabricated, cyclic voltammograms, electrochemical surface area (ECSA) and catalyst utilization are measured. The *in-situ* cyclic voltammetry (CV) analyses are performed by using a commercial fuel cell test station (Greenlight Innovation, G20), connected to the booster and frequency response analyzer modules (Gamry Instruments, 30K); humidified hydrogen and nitrogen are supplied to the anode (the reference and also the counter electrode) and cathode (working electrode) of the cell, respectively. The CV measurements are carried out by varying the voltage applied between 0.10 and 0.80 V, with a scanning rate of 0.05 V/s, with at least 25 cycles. The relative standard deviation of the ECSA presented is less than 3%. A detailed calculation base for both the ECSA and catalyst utilization can be found in [32,33].

2.6. Single cell performance testing

Cell performance characteristics of the MEAs are investigated using a fuel cell test station with a single scaled-up cell having an electrode geometric active area of 45 cm^2 . The test MEA is first assembled between the anode and cathode flow-field plates, then performance test is carried out under different operating conditions, such as varied RHs and flow rates of air and hydrogen streams. To obtain the steady-state polarization curve, the current density is measured potentiostatically from open-circuit voltage (OCV) to the cell voltage of about 0.30

V, with 0.10 V decrements. The current density values are recorded upon establishment of the steady-state conditions, which typically takes about 5 min. Each polarization curve presented in this work represents the average of three polarization curves obtained at different times and days, with a standard deviation of about 5%.

3. Results and Discussion

3.1. Morphological and microstructural analyses

The surface morphologies of the anode and cathode GDLs and CLs of the proposed MEA design are investigated through scanning electron microscopy (SEM) imaging, as presented in Figs. 1 and 2. It is seen that the anode GDL possesses a rather compact and porous surface morphology, comprised of homogeneously distributed carbon powder/hydrophobic agent agglomerates (see Figs. 1(a) and 1(b)). In some locations, there are also visible macro-scale holes and surface cracks, likely formed due to the specifications of either the carbon powder employed (i.e., small average particle size) or manufacturing process (i.e., pore-forming agent introduction and/or drying and sintering conditions), and are expected to provide straight pathways for the mass transport. In the cathode GDL, as seen from Figs. 1(c) and 1(d), the macro-scale flake-like graphene particles disperse homogeneously and build up a compact and thin network (10-15 μm) on the surface of the single-layer GDL. In some regions, probably due to the superfine architecture of the graphene-based MPL, the randomly oriented carbon fibres of the single-layer GDL are also visible, particularly in these regions, the presence of the macro-scale pores is clear; these pores can provide straight pathways and facilitate water removal, especially under high-humidity conditions. Apart from these macro-scale holes, such a superfine, compact, and smooth MPL is expected to provide a good platform for the CCL, thereby improving catalyst activity and catalyst utilization by preventing the penetration of Pt particles into the single-layer GDL.

In the anode catalyst layer (ACL), as evident in Figs. 2(a) and 2(b), the Pt/C particles bound to each other by the ionomer (which is shown as white particles) appear to yield a homogeneous distribution without any visible ionomer agglomeration throughout the surface. As a matter of fact, such a compact, homogeneous, and porous surface morphology is quite desirable. Dark regions, which are particularly visible in Fig. 2(b), represent the nano-scale pores within the ACL and are expected to facilitate reactant transport to the electrochemical reaction regions. The surface morphology of the ACL is akin to that of the anode GDL, as there are relatively more void regions, potentially originating from the relatively low catalyst loading (0.10 mg/cm^2). In the CCL, the Pt/C particles, as seen in Figs. 2(c) and 2(d), tend to bind to each other and form agglomerates composed of multiple particles, attributable to the presence of ionomer, but these agglomerates are quite small (mostly comprised of several Pt/C particles) and distributed rather homogeneously throughout the surface. The CCL also seems to be abundant, with nano-scale pores distributed homogeneously throughout the surface; clearly the pores present in the CCL are relatively smaller than those in the ACL, attributable to the relatively higher cathode catalyst loading (0.40 mg/cm^2). Such a CCL morphology and microstructure is quite desirable, because there are many pathways that can ensure good distribution of the reactant molecules over the electrochemically active regions, as well as facilitate removal of the saturated water from the three-phase boundary in an effective manner. It is also worth mentioning that the graphene-based MPL employed on the cathode electrode seems to provide a quite proper platform for the CCL, as the obtained CCL morphology is very smooth and homogenous; such a good platform is likely to positively affect the catalyst activity and catalyst utilization characteristics of the MEA.

The microstructural characteristics of the porous components of the proposed MEA design, i.e., single-layer GDL, anode and cathode GDLs, and anode and cathode electrodes, are presented in Table 1. To ensure proper comparison between the pore characteristics of the

investigated components and provide insights into these components' capability in dealing with mass transport, pores inside the components are classified into three categories according to their diameter d : micropores ($d \leq 0.07 \mu\text{m}$), mesopores ($0.07 \mu\text{m} \leq d \leq 5 \mu\text{m}$), and macropores ($5 \mu\text{m} \leq d$). Such categorization is very common in the fuel cell literature; for example, see [34,35]. However, the ranges identified here may differ from any other identification of micro-, meso-, and macropores.

To understand the microstructural characteristics obtained upon deposition of the graphene MPL, we first investigate the pore characteristics of the single-layer GDL employed as the sublayer of the cathode GDL. For the single-layer GDL, the pores classified as micro-, meso-, and macropores make up almost 5.3%, 43.2%, and 51.5% of the total porosity, respectively. The relatively higher volume of meso- and macro-pores could be ascribed to the presence of the large numbers of macro-scale pores inside the carbon matrix; and these macro-scale pores are formed likely due to the network constructed by the randomly aligned carbon fibers. The relatively small micro-pore volume could result from the nano-scale spaces at the carbon fiber/carbon fiber and/or carbon-fiber/polymeric binder interfaces. The relatively higher meso- and macro- and smaller micro-pore volumes of the single-layer GDL correspondingly give rise to a comparatively higher mean pore size and total porosity: 194.2 nm and 74.9%, respectively. Since almost 74.9% of bulk volume is taken up by the pores, the bulk density of the single-layer GDL is reasonably small, around 0.2209 g/cm^3 .

For the cathode GDL, approximately 7.4% of the pore volume is taken up by the micropores, while 54.8% and 37.8% are taken up by the meso- and macropores, respectively (Table 1). The pore characteristics of the single-layer GDL seem to show great variation upon deposition of the graphene MPL onto it; obviously, the deposition of the graphene MPL brings about a notable increase in the micro- and meso-pore volume, but a significant drop in the macro-pore

volume. The increase in the micro- and meso-pore volumes could be related to the newly formed comparatively small-scale pores at the interfaces of graphene particles/hydrophobic agent/carbon fibers. With the formation of these small-scale pores, both the mean pore size and porosity demonstrate a noticeable drop, from 194.2 nm to 170.3 nm and 74.9% to 67.1%, respectively. However, as is clear from the SEM image of the graphene MPL (see Fig. 1(c)), there are still visible macro-scale pores, which are potentially the main contributors to the macro-pore volume (37.8%). As mentioned earlier, the graphene flakes tend to penetrate into the open pores of the single-layer GDL, in particular into those near the surface; such a penetration pattern may explain the reduced macro- and increased micro- and meso-pore volumes. However, the presence of a relatively large macro-pore volume upon graphene MPL deposition implies that the graphene flakes present a superficial penetration profile – the flakes tend to accumulate in the open pores near the surface rather than penetrate deeply into them. This penetration pattern can be ascribed to the flake-like shape and comparatively large nominal particle size of graphene (40 μm). This inference can also be corroborated by the SEM images of the graphene MPL (see Figs. 1(c) and 1(d)). Further, with the deposition of the graphene MPL, the bulk density is seen to increase from 0.2209 g/cm^3 to 0.2810 g/cm^3 , attributable to the presence of the extra layer (MPL).

The deposition of the CCL onto the cathode GDL increases the micro-pore volume from 7.4% to 16.9%, while reducing the meso- and macro-pore volume from 54.8% to 51.8% and 37.8% to 31.3%, respectively (Table 1). Such a trend is quite reasonable when considering that the CCL is composed of ~ 3 nm Pt particles, ~ 30 nm carbon particles, and ~ 10 nm ionomer films, and that the pores formed at the interface of these three materials will reasonably be in the micro-pore category. The presence of these micropores is also clearly seen from the SEM images of the CCL (see Figs. 2(c) and 2(d)). Besides the pores formed at the interfaces, the inherently porous structure of the carbon particles (on which Pt nanoparticles are dispersed)

may also contribute to the relatively higher micro-pore volume. With the deposition of the CCL, the porosity is seen to decrease from 67.1% to 63.8%, consistent with the formation of more micro-pores. The cumulative surface area of the cathode electrode is also substantially higher than the cathode GDL, indicating that the micropores are the major contributor to the pore surface area. The mean pore sizes obtained for the cathode GDL and cathode electrode are 170.3 nm and 120.3 nm, respectively, a difference in good agreement with the above discussion. Lastly, the bulk density of the cathode GDL increases with the deposition of the CCL from 0.2810 g/cm³ to 0.3843 g/cm³ – which is reasonable when considering that the cathode electrode contains an extra layer (CCL).

In the anode GDL, almost 14.4% of the pore volume is in the micro-pore category, 47.5% is in the meso-pore category, and 38.1% is in the macro-pore category. Such a pore size distribution is quite reasonable, particularly when considering the volume of each pore category in the single-layer GDL – namely, it has relatively higher micro- and meso-pore volumes but a lower macro-pore volume. The higher volume of micro- and mesopores is potentially related to the relatively small-scale pores formed at the interfaces of carbon powder/hydrophobic agent agglomerates in the anode MPL. The reduction in the macro-pore volume could be ascribed to the penetration of carbon powder/hydrophobic agent agglomerates partially into the single-layer GDL. The anode GDL has a relatively smaller porosity and mean pore size but a higher cumulative pore surface area than the single-layer GDL, potentially attributable to the higher micro- and meso-pore volume existing in the anode GDL. As the anode GDL possesses an additional layer (MPL), its bulk density is correspondingly higher than the single-layer GDL (Table 1).

The deposition of the ACL onto the anode GDL results in a slight increase in the micro-pore volume, with a slight decrease in the meso- and macro-pore volumes. This trend indicates that the Pt-C/ionomer agglomerates in the ACL lead to the formation of small-scale pores, and

these newly formed pores result in an increase in the micro-pore volume while decreasing the meso- and macro-pore volumes. These small-scale pores formed upon ACL deposition are also clearly seen in the SEM images (Figs. 2(a) and 2(b)). It is also worth noting that the deposition of the ACL onto the anode GDL brings about only slight microstructural changes, compared to that of the CCL onto the cathode GDL. This trend can be explained by the differences in the catalyst loadings in the anode (0.10 mg/cm^2) and cathode (0.40 mg/cm^2) electrodes. The relatively lower catalyst loading in the ACL potentially causes the formation of fewer micropores, and hence the contribution of these fewer micropores to the overall electrode microstructure is inevitably limited. In consequence, all the other parameters recorded for the anode electrode, such as mean pore size, total porosity, total pore volume, total pore surface area, and bulk density, are rather close to those obtained from the anode GDL (Table 1).

3.2. Physical analyses

A summary of the physical characteristics of the porous cell components, i.e., anode and cathode GDLs and electrodes, employed in the proposed MEA design is presented in Table 2.

The through-plane gas permeability coefficients of the anode and cathode GDLs and electrodes employed in the proposed MEA design are determined to understand these porous components' capability in dealing with convection governed mass transport. As is clear from Table 2, the through-plane gas permeability coefficient of the single-layer GDL employed as the sublayer of the cathode electrode is obtained as $(6.22-7.11) \times 10^{-12} \text{ m}^2$, which is far smaller than those calculated for the cathode GDL $((9.17-9.64) \times 10^{-14} \text{ m}^2)$ and cathode electrode $((2.17-2.31) \times 10^{-14} \text{ m}^2)$. Likewise, the through-plane gas permeability coefficient of the anode GDL $((1.33-1.41) \times 10^{-13})$ is more than 2 times higher than that of the anode electrode $((5.92-6.11) \times 10^{-14})$. Such a trend is quite reasonable when considering that the through-plane gas

permeability of a porous cell component depends greatly on that component's morphological and microstructural characteristics, as these characteristics have a decisive influence on the complexity of the diffusional pathways in the through-plane direction. For example, macro-level holes and surface cracks in a porous component are likely to provide more straight pathways, through which gas-phase reactants can flow without experiencing significant resistance. Similarly, a porous component with a high porosity, mean pore size, and macro-pore volume can reasonably possess broad pathways, through which reactant flow occurs in an effective manner.

Building on this, the through-plane gas permeability characteristics considered in this section should be discussed in relation to their morphological and microstructural characteristics. The higher macro-pore volume in the single-layer GDL seems to provide wider and less-complex pathways, because its through-plane gas permeability coefficient is far higher than those of the anode and cathode GDLs. This finding indicates that deposition of the MPLs onto the single-layer GDL increases the complexity (tortuosity) of the diffusion pathways in the through-plane direction. The relatively higher complexity of the anode and cathode GDLs could be attributed to their noticeably higher micro- and meso-pore volumes than the single-layer GDL. Due to the comparatively intricate network constructed by these small-scale pores, the molecules of the working fluid (air in the present case) unavoidably follow an indirect route (comprised of rather narrow diffusional pathways) to traverse these porous components, meaning that gas molecules potentially face significant resistance.

It is also seen that the composition of the MPL directly influences the gas permeability characteristics of the resulting GDL. The strong evidence that supports this hypothesis is the clear differences between the gas permeability coefficients of the anode and cathode GDLs; for example, a relatively higher gas permeability of the anode GDL. As a matter of fact, this finding is quite interesting, and is essential to understand the unique morphology of the

graphene-based MPL employed in the cathode GDL, such that even though the micro-pore volume in the cathode GDL (7.4%) is nearly half that in the anode GDL (14.4%), the anode GDL yields relatively higher through-plane gas permeability. This trend could be ascribed to the dissimilarities in the morphological characteristics of the anode and cathode GDLs. For example, in the cathode GDL, the MPL comprised of firmly and horizontally packaged flake-like graphene particles seems to create a larger barrier to the working fluid flowing in the perpendicular direction; or alternatively, the surface cracks and holes on the surface of the anode GDL could offer straight pathways through which the working fluid flows directly. Owing to its unique morphology, graphene-based MPL is expected to provide effective water retention capability to the cathode electrode, in particular under dry and/or partially humidified conditions. Lastly, it is also clear that deposition of both the ACL and CCL results in a noticeable drop in the through-plane gas permeability coefficients (Table 2). This finding is reasonable when considering that the CL is mostly composed of micro-scale pores, namely it has a rather intricate microstructure, and hence a significant barrier to the air flow. However, deposition of the CCL onto the cathode GDL appears to cause a comparatively sharper decline in the gas-permeability coefficient, compared to that of the ACL onto the anode GDL, attributable to the higher catalyst loading on the cathode electrode.

The surface wettability characteristics of the porous components are also investigated through static contact angle measurements, to provide practical insights into their water management characteristics. As clearly seen from Table 2, the single-layer GDL yields a relatively lower and broader static contact angle ($144\text{-}150^\circ$) range than either the anode ($152\text{-}156^\circ$) or cathode ($150\text{-}154^\circ$) GDLs, potentially related to the differences in the morphological and microstructural characteristics of the components under investigation. For instance, as mentioned earlier, the single-layer GDL is composed of arbitrarily aligned carbon fibers that lie in the in-plane direction, and hence it has a rather heterogeneous surface morphology

comprised of open pores with diameters up to 150 μm . The heterogeneous pore size distribution on the surface (hence inhomogeneous surface morphology) could result in large variations in the surface wettability characteristics – this could be the main reason of the broader static contact angle range noted for the single-layer GDL. However, the reason for the relatively lower static contact angle of the single-layer GDL could be the large size of the pores on the surface. According to the Young-Laplace correlation, the presence of such open pores on the surface could give rise to a lower surface capillarity (since the wettability of a pore is reversely proportional to its pore radius [35]), and thus the water droplets dropped onto the surface of the single-layer GDL are prone to penetrate into these open pores, giving rise to a relatively lower static contact angle. In the anode and cathode GDLs, the presence of the MPL composed of relatively small pores on the surface leads to a relatively more hydrophobic and uniform surface morphology, and hence a comparatively higher static contact angle with a smaller range (Table 2). It is also clear that the anode GDL yields slightly higher hydrophobic surface characteristics than the cathode GDL, attributable to the relatively higher micro-pore volume in the anode GDL. As evident from Table 2, upon deposition of both the ACL and CCL, the surface wettability characteristics of the electrodes appear to become more homogeneous and relatively more hydrophobic – this finding is quite interesting, because both the ACL and CCL contain a polymeric binder, an inherently hydrophilic material. However, it seems that the nano-scale pores in the CLs have a more decisive impact on the overall surface wettability characteristics; or alternatively, any potential contribution to the surface hydrophilicity due to the presence of the polymeric binder is successfully compensated for by the hydrophobicity introduced by the nano-scale pores.

3.3. Cyclic Voltammetry analysis

Cyclic voltammograms (CVs) for hydrogen adsorption and desorption peaks are determined to understand the electrochemical characteristics of the proposed MEA design, as presented in

Fig. 3. The CV has a shape common with those obtained in the literature for the MEAs of PEM fuel cells; for example, see [36,37]. As mentioned earlier, the ECSA of the proposed MEA design is also calculated by utilizing three elements: the amount of hydrogen adsorption and desorption charges, the amount of Pt loading used in the cathode electrode, and the fixed value of the electrical charge associated with the monolayer adsorption of hydrogen on a Pt surface [32,33]. The ECSA of the MEA is found to be 58.0 m²/g, which is promising, when considering the ECSAs of the MEA designs investigated in recent years (see [38–41], for example). The relatively higher ECSA for the MEA may be related to two potential reasons. The first is the comparatively faster electron transport, and hence faster hydrogen desorption reaction rate, ensured by the advanced electron transport capability of the graphene-based MPL employed in the cathode electrode. The second, however, is the higher degree of surface contact, ensured by the smooth and homogeneous surface morphology of the graphene-based MPL, in which graphene flakes are firmly and horizontally packaged (see Fig. 1(c)). The catalyst utilization of the MEA is also determined by dividing the previously calculated ECSA with the theoretically calculated ones through the correlation provided in [26]. The catalyst utilization of the MEA is calculated to be 62.0%; such a catalyst utilization percentage is quite promising, when considering the catalyst utilization percentages reported for the MEAs investigated recently in the open literature (see [42], for example).

3.4. Single cell performance analysis

Single-cell performance analyses of the proposed MEA design are conducted to assess its performance characteristics under different flow rates and relative humidities (RHs) of air and hydrogen streams; and a detailed discussion on the obtained performance characteristics is provided by considering the performance targets set by the DOE for 2020 as well as the recently published studies in the open literature.

Figures 4(a) and 4(b) present the steady-state current voltage (I-V, polarization) and power density curves of the proposed MEA design under different flow conditions of the fully humidified air and hydrogen streams. For brevity, the flow rates of the hydrogen and air reactant streams investigated are broken into three categories: low flow, moderate flow, and high flow. The high-, moderate-, and low-flow conditions represent the hydrogen and air flow rates of 4.45 and 9.00 L/min, hydrogen/air with the stoichiometric ratios of 1.20 and 4.00, and hydrogen/air with the stoichiometric ratios of 1.20 and 2.00, respectively. Obviously, the MEA shows similar performance under different flow conditions, namely low-, moderate-, and high-flow conditions. The open circuit voltages (OCVs) recorded are around 0.95 V under these three conditions. The activation polarization dominated region performance characteristics are seen to be very close to each other at the low-, moderate-, and high-flow conditions; more specifically, at the constant current density of 0.30 A/cm², the cell voltages obtained under the low-, moderate-, and high-flow conditions are 0.769 V, 0.783 V, and 0.785 V, respectively. These characteristics also appear to be highly promising, particularly when considering the current density targets of 0.24 A/cm² and 0.30 A/cm² at the cell voltage of 0.80 V established by the DOE for 2015 and 2020, respectively [43]. Clearly, the proposed MEA design has already met the activation region performance expectations for 2015, and offers a great promise of meeting those for 2020. The insensitive trend to the varying flow conditions is also valid for the ohmic region (or at the intermediate current densities) – for example, at the constant cell voltage of 0.60 V, almost the same current density of 1.50 A/cm² is achieved under the low-, intermediate-, and high-flow conditions. However, in the concentration polarization dominated region, i.e., at the current density of 2.50 A/cm², the cell voltage is seen to decrease by only 3.50% as the flow condition is changed from high- to low-flow. Since the performance losses in the ohmic region are an indicator of the cell resistance (which is in turn dominated by the membrane resistance), the similarities in the performance

characteristics clearly demonstrate that the MEA is quite insensitive to changes in the flow conditions investigated, or it can successfully tolerate the variations in the humidification level associated with the changing multi-phase flow characteristics. More specifically, the MEA seems to be well-hydrated independent of flow conditions – quite a desirable finding when considering the operational flexibility targets established by the DOE for 2020 [43]. As a matter of fact, the MEA also yields almost identical performance characteristics at the concentration polarization dominated region under different flow conditions; more specifically, the maximum power densities obtained under low-, moderate-, and high-flow conditions are 1.094 W/cm², 1.134 W/cm², and 1.137 W/cm², respectively.

Figures 5(a) and 5(b) provide the polarization and power density curves of the proposed MEA design under different flow conditions of the partially humidified (70% RH) air and hydrogen streams. As clearly seen from Fig. 5(a), the MEA presents similar performance characteristics under the activation, ohmic, and concentration polarization dominated regions of the polarization curves. For example, at the constant current density of 0.30 A/cm², the cell voltages noted under the low-, moderate-, and high-flow conditions are 0.739 V, 0.728 V, and 0.761 V, respectively. The performance similarities in the activation polarization dominated region indicate that the anodic and cathodic reactions are only slightly affected by the operating conditions. It is also seen that the reduction in the RHs of the hydrogen and air streams (from 100% to 70%) causes a slight decrease in the cell performance under all the flow conditions. This decay in the activation regional performance is an indicator of the reduction in the anodic and cathodic reaction kinetics, potentially resulting from the dehydration-dependent reduction in the three-phase boundary. The performance characteristics at the ohmic and concentration dominated regions are also quite similar under different flow conditions at 70% RH. For example, at the fixed cell voltage of 0.60 V, the current density achieved is about 1.15 A/cm² for the low-, moderate-, and high-flow

conditions at 70% RH. Even though the cell experiences a noticeable drop in the overall ohmic region performance compared to the fully-humidified conditions, the performance is still highly satisfactory when considering the performances of the cells operating at partially humidified conditions reported in the open literature; for example, see [44,45]. Likewise, the similarity in the performance characteristics is also observed in the concentration polarization dominant region; more specifically, the peak power densities under the low-, moderate-, and high-flow conditions at 70% RH are 0.877 W/cm², 0.928 W/cm², and 0.879 W/cm², respectively (Fig. 5(b)). The difference between the peak power densities obtained is no more than 5.5%, confirming clearly the insensitivity of the MEA to the flow conditions.

As seen from Figs. 6(a) and 6(b), for further reduction in the RHs of air and hydrogen streams (from 70% to 40%), the cell performance seems to further deteriorate, and the differences between the performance characteristics for low-, moderate-, and high-flow conditions become more visible. Even though the overall performance deteriorates, the cell still provides highly promising performance, when considering the previously reported cell performances for low-humidity conditions – for example, see [44,46]. On the other hand, unlike the performance characteristics noted for the relatively higher humidification levels (such as, for 70% and 100% RHs), the cell seems to perform noticeably better at 40% RH, as the hydrogen and air are supplied to the cell with the low-flow condition mode. This performance trend is quite interesting, because normally the higher flow rates of the reactants are expected to provide higher reactant availability, and the cell is expected not to experience any deterioration in the performance due to reactant starvation. However, here, we demonstrate that the cell can perform quite differently, as the reactants are supplied to the cell with lower RHs (i.e., 40%). Here, the supply of partially humidified (40%) reactants under the high-flow condition seems to cause severe dehydration in the ionomer and membrane, consistent with the comparatively higher slope of the linear part of the polarization curve obtained for the

high-flow condition (see Fig. 6(a)). These performance characteristics imply that the proposed MEA design provides effective water preservation under low-humidity conditions without the need of a high-flow condition reactant supply. The water retention capability of the MEA could originate from the presence of the compact graphene-based MPL, by which sufficient water can be easily absorbed inside the cell, and correspondingly a sufficient level of humidification can be maintained even under low-humidity operation.

In summary, as is clear in Fig. 7, the MEA exhibits the best performance at the fully-humidified condition (100% RH) independent of flow conditions investigated, and the peak power densities achieved for the low-, moderate-, and high-flow conditions under this humidification are very close to each other. For example, the peak power densities obtained under low-, moderate-, and high-flow conditions are 1.094 W/cm², 1.134 W/cm², and 1.137 W/cm², respectively. When the RHs of air and hydrogen streams are decreased to 70%, the MEA seems to sustain its performance characteristics, regardless of flow conditions; however, the peak power densities obtained under low-, moderate-, and high-flow conditions at 70% RH seem to be relatively far from each other, compared to those noted at 100% RH. More specifically, the peak power densities obtained from the MEA at 70% RH under low-, moderate-, and high-flow conditions are 0.877 W/cm², 0.928 W/cm², and 0.879 W/cm², respectively. Interestingly, the MEA yields comparatively higher peak power density under moderate-flow condition (rather than high-humidity condition), as the air and hydrogen RHs are decreased from 100% to 70%. This trend clearly shows the presence of antagonistic relationship between membrane hydration and water flooding, such that when the reactants are supplied to the cell at 100% RH, the MEA seems to suffer relatively more from water flooding, and in this case, the supply of fully-humidified reactants under high-flow conditions to the cell seems to facilitate excess water removal from the cell while providing sufficient humidification for the ionomer and membrane. Such an effective balance between water

removal and membrane and ionomer humidification in turn gives rise to a relatively higher peak power density. However, the supply of partially humidified (70% RH) to the cell appears to induce slight dehydration of the membrane and ionomer, and hence dehydration-dependent performance losses inevitably emerge. For further decrease in the RHs (from 70% to 40%), the peak power densities under low-, moderate-, and high-flow conditions are recorded to be 0.777 W/cm², 0.699 W/cm², and 0.548 W/cm², respectively. Herein, the MEA seems to experience more severe dehydration-dependent performance losses, particularly when the reactants are supplied to the cell with moderate- and high-flow conditions, potentially attributable to the drying effect of the reactants on the membrane and ionomer. These findings clearly indicate that the proposed MEA can establish an effective balance between membrane hydration and water removal even under quite severe operation conditions (i.e., low-humidity and low-flow conditions).

4. Conclusions

In this study, a membrane electrode assembly (MEA) that is suitable for a wide range of humidification and flow conditions is developed for proton exchange membrane (PEM) fuel cells. In the proposed MEA, a microporous layer (MPL) made of graphene is employed on the cathode electrode, catalyst layers (CLs) comprised of a short-side-chain (SSC) ionomer are employed on the anode and cathode electrodes, and an electrolyte composed of a SSC ionomer is employed as the membrane. The porous components of the proposed MEA are characterized through morphological, microstructural, physical, and electrochemical characterizations. Single and scaled-up performance characteristics of the MEA are investigated under a wide range of flow conditions and relative humidities of the air and hydrogen streams. The results indicate that the graphene-based MPL has a unique morphology and microstructure that not only improve water management, but also promote catalyst activity and catalyst utilization. Owing to this unique morphology and microstructure,

the graphene-based MPL serves as a valve that prevents water removal under low-humidity operation, improving the water retention capability of the MEA. This capability in turn makes the MEA highly suitable for low-humidity operation. The high insensitivity of the SSC ionomer to humidification imparts further insensitivity to the operating conditions. The SSC ionomer based CLs are found to provide a highly porous microstructure for the CLs, which in turn enables the electrodes to have relatively higher through-plane gas permeability. Owing to all these favorable characteristics, the MEA presents stable and highly promising performance, regardless of flow conditions under different humidification levels.

5. Acknowledgements

This work has been financially supported by the Ontario-China Research and Innovation Fund (OCRIF Round 3), the Natural Sciences and Engineering Research Council of Canada (NSERC) via a Discovery Grant, and conducted as part of the Catalysis Research for Polymer Electrolyte Fuel Cells (CaRPE FC) Network administered from Simon Fraser University and supported by Automotive Partnership Canada (APC) Grant No. APCPJ 417858 - 11 through the Natural Sciences and Engineering Research Council of Canada (NSERC). We would also like to acknowledge Group NanoXplore Inc. for supply of graphene powder (heXo-G V20) for the manufacturing of graphene-based microporous layer (MPL) employed in the cathode electrode of the membrane electrode assembly (MEA) investigated in this study.

References

- [1] Munavalli BB, Naik SR, Kariduraganavar MY. Development of robust proton exchange membranes for fuel cell applications by the incorporation of sulfonated β -cyclodextrin into crosslinked sulfonated poly(vinyl alcohol). *Electrochimica Acta* 2018;286:350–64. doi:10.1016/j.electacta.2018.08.036.
- [2] Gao S, Xu H, Fang Z, Ouadah A, Chen H, Chen X, et al. Highly sulfonated poly(ether ether ketone) grafted on graphene oxide as nanohybrid proton exchange membrane applied in fuel cells. *Electrochimica Acta* 2018;283:428–37. doi:10.1016/j.electacta.2018.06.180.

- [3] Zhang L, Wilkinson DP, Liu Y, Zhang J. Progress in nanostructured (Fe or Co)/N/C non-noble metal electrocatalysts for fuel cell oxygen reduction reaction. *Electrochimica Acta* 2018;262:326–36. doi:10.1016/j.electacta.2018.01.046.
- [4] Qi Z, Kaufman A. Improvement of water management by a microporous sublayer for PEM fuel cells. *Journal of Power Sources* 2002;109:38–46. doi:10.1016/S0378-7753(02)00058-7.
- [5] Hou S, Chi B, Liu G, Ren J, Song H, Liao S. Enhanced performance of proton exchange membrane fuel cell by introducing nitrogen-doped CNTs in both catalyst layer and gas diffusion layer. *Electrochimica Acta* 2017;253:142–50. doi:10.1016/j.electacta.2017.08.160.
- [6] Cho MK, Park H-Y, Lee SY, Lee B-S, Kim H-J, Henkensmeier D, et al. Effect of Catalyst Layer Ionomer Content on Performance of Intermediate Temperature Proton Exchange Membrane Fuel Cells (IT-PEMFCs) under Reduced Humidity Conditions. *Electrochimica Acta* 2017;224:228–34. doi:10.1016/j.electacta.2016.12.009.
- [7] Oh H, Park J, Min K, Lee E, Jyoung JY. Effects of pore size gradient in the substrate of a gas diffusion layer on the performance of a proton exchange membrane fuel cell. *Applied Energy* 2015;149:186–93. doi:10.1016/j.apenergy.2015.03.072.
- [8] Ito H, Heo Y, Ishida M, Nakano A, Someya S, Munakata T. Application of a self-supporting microporous layer to gas diffusion layers of proton exchange membrane fuel cells. *Journal of Power Sources* 2017;342:393–404. doi:10.1016/j.jpowsour.2016.12.064.
- [9] Kitahara T, Nakajima H, Morishita M. Water vapor exchange system using a hydrophilic microporous layer coated gas diffusion layer to enhance performance of polymer electrolyte fuel cells without cathode humidification. *Journal of Power Sources* 2012;214:100–6. doi:10.1016/j.jpowsour.2012.04.067.
- [10] Chi B, Hou S, Liu G, Deng Y, Zeng J, Song H, et al. Tuning hydrophobic-hydrophilic balance of cathode catalyst layer to improve cell performance of proton exchange membrane fuel cell (PEMFC) by mixing polytetrafluoroethylene (PTFE). *Electrochimica Acta* 2018;277:110–5. doi:10.1016/j.electacta.2018.04.213.
- [11] Utaoka Y, Koresawa R. Effect of wettability-distribution pattern of the gas diffusion layer with a microgrooved separator on polymer electrolyte fuel cell performance. *Journal of Power Sources* 2017;363:227–33. doi:10.1016/j.jpowsour.2017.07.095.
- [12] Lapique F, Belhadj M, Bonnet C, Pauchet J, Thomas Y. A critical review on gas diffusion micro and macroporous layers degradations for improved membrane fuel cell durability. *Journal of Power Sources* 2016;336:40–53. doi:10.1016/j.jpowsour.2016.10.037.
- [13] Najafabadi AT, Leeuwner MJ, Wilkinson DP, Gyenge EL. Electrochemically Produced Graphene for Microporous Layers in Fuel Cells. *ChemSusChem* 2016;9:1689–97. doi:10.1002/cssc.201600351.
- [14] Leeuwner MJ, Wilkinson DP, Gyenge EL. Novel Graphene Foam Microporous Layers for PEM Fuel Cells: Interfacial Characteristics and Comparative Performance. *Fuel Cells* 2015;15:790–801. doi:10.1002/fuce.201500031.
- [15] Chen HH, Chang MH. Effect of cathode microporous layer composition on proton exchange membrane fuel cell performance under different air inlet relative humidity. *Journal of Power Sources* 2013;232:306–9. doi:10.1016/j.jpowsour.2013.01.079.

- [16] Chun JH, Park KT, Jo DH, Lee JY, Kim SG, Lee ES, et al. Determination of the pore size distribution of micro porous layer in PEMFC using pore forming agents under various drying conditions. *International Journal of Hydrogen Energy* 2010;35:11148–53. doi:10.1016/j.ijhydene.2010.07.056.
- [17] Kitahara T, Nakajima H, Mori K. Hydrophilic and hydrophobic double microporous layer coated gas diffusion layer for enhancing performance of polymer electrolyte fuel cells under no-humidification at the cathode. *Journal of Power Sources* 2012;199:29–36. doi:10.1016/j.jpowsour.2011.10.002.
- [18] Ito H, Iwamura T, Someya S, Munakata T, Nakano A, Heo Y, et al. Effect of through-plane polytetrafluoroethylene distribution in gas diffusion layers on performance of proton exchange membrane fuel cells. *Journal of Power Sources* 2016;306:289–99. doi:10.1016/j.jpowsour.2015.12.020.
- [19] Ahn M, Cho YH, Cho YH, Kim J, Jung N, Sung YE. Influence of hydrophilicity in microporous layer for polymer electrolyte membrane fuel cells. *Electrochimica Acta* 2011;56:2450–7. doi:10.1016/j.electacta.2010.11.063.
- [20] Carton JG, Lawlor V, Olabi a. G, Hochenauer C, Zauner G. Water droplet accumulation and motion in PEM (Proton Exchange Membrane) fuel cell mini-channels. *Energy* 2012;39:63–73. doi:10.1016/j.energy.2011.10.023.
- [21] Rezaei Niya SM, Hoorfar M. Study of proton exchange membrane fuel cells using electrochemical impedance spectroscopy technique - A review. *Journal of Power Sources* 2013;240:281–93. doi:10.1016/j.jpowsour.2013.04.011.
- [22] Ozden A, Ercelik M, Devrim Y, Colpan CO, Hamdullahpur F. Evaluation of sulfonated polysulfone/zirconium hydrogen phosphate composite membranes for direct methanol fuel cells. *Electrochimica Acta* 2017;256:196–210. doi:10.1016/j.electacta.2017.10.002.
- [23] Ozden A, Ercelik M, Ozdemir Y, Devrim Y, Colpan CO. Enhancement of direct methanol fuel cell performance through the inclusion of zirconium phosphate. *International Journal of Hydrogen Energy* 2017:1–17. doi:10.1016/j.ijhydene.2017.01.188.
- [24] Ercelik M, Ozden A, Devrim Y, Colpan CO. Investigation of Nafion based composite membranes on the performance of DMFCs. *International Journal of Hydrogen Energy* 2016;42:2658–68. doi:10.1016/j.ijhydene.2016.06.215.
- [25] Ozden A, Shahgaldi S, Zhao J, Li X, Hamdullahpur F. Assessment of graphene as an alternative microporous layer material for proton exchange membrane fuel cells. *Fuel* 2018;215:726–34. doi:10.1016/j.fuel.2017.11.109.
- [26] Ozden A, Shahgaldi S, Li X, Hamdullahpur F. A graphene-based microporous layer for proton exchange membrane fuel cells: Characterization and performance comparison. *Renewable Energy* 2018;126:485–94. doi:10.1016/j.renene.2018.03.065.
- [27] Park YC, Kakinuma K, Uchida H, Watanabe M, Uchida M. Effects of short-side-chain perfluorosulfonic acid ionomers as binders on the performance of low Pt loading fuel cell cathodes. *Journal of Power Sources* 2015;275:384–91. doi:10.1016/j.jpowsour.2014.10.149.
- [28] Shahgaldi S, Alaefour I, Zhao J, Li X. Impact of ionomer in the catalyst layers on proton exchange membrane fuel cell performance under different reactant flows and pressures. *Fuel* 2018;227:35–41. doi:10.1016/j.fuel.2018.04.076.

- [29] Shahgaldi S, Alaefour I, Li X. The impact of short side chain ionomer on polymer electrolyte membrane fuel cell performance and durability. *Applied Energy* 2018;217:295–302. doi:10.1016/j.apenergy.2018.02.154.
- [30] Zhao J, Ozden A, Shahgaldi S, Alaefour IE, Li X, Hamdullahpur F. Effect of Pt loading and catalyst type on the pore structure of porous electrodes in polymer electrolyte membrane (PEM) fuel cells. *Energy* 2018;150:69–76. doi:10.1016/j.energy.2018.02.134.
- [31] Zhao J, Shahgaldi S, Alaefour I, Xu Q, Li X. Gas permeability of catalyzed electrodes in polymer electrolyte membrane fuel cells. *Applied Energy* 2018;209:203–10. doi:10.1016/j.apenergy.2017.10.087.
- [32] Song S, Wang Y, Shen PK. Pulse-microwave assisted polyol synthesis of highly dispersed high loading Pt/C electrocatalyst for oxygen reduction reaction. *Journal of Power Sources* 2007;170:46–9. doi:10.1016/j.jpowsour.2007.04.012.
- [33] You DJ, Kwon K, Joo SH, Kim JH, Kim JM, Pak C, et al. Carbon-supported ultra-high loading Pt nanoparticle catalyst by controlled overgrowth of Pt: Improvement of Pt utilization leads to enhanced direct methanol fuel cell performance. *International Journal of Hydrogen Energy* 2012;37:6880–5. doi:10.1016/j.ijhydene.2012.01.103.
- [34] Tseng C-J, Lo S-K. Effects of microstructure characteristics of gas diffusion layer and microporous layer on the performance of PEMFC. *Energy Conversion and Management* 2010;51:677–84. doi:10.1016/j.enconman.2009.11.011.
- [35] Wang X, Zhang H, Zhang J, Xu H, Zhu X, Chen J, et al. A bi-functional micro-porous layer with composite carbon black for PEM fuel cells. *Journal of Power Sources* 2006;162:474–9. doi:10.1016/j.jpowsour.2006.06.064.
- [36] Kumpulainen H, Peltonen T, Koponen U, Bergelin M, Valkiainen M, Wasberg M. In situ voltammetric characterization of PEM fuel cell catalyst layers. *VTT Tied - Valt Tek Tutkimusk* 2002:3–28.
- [37] Gouws S. Voltammetric Characterization Methods for the PEM Evaluation of Catalysts. *Electrolysis* 2012. doi:10.5772/48499.
- [38] Shahgaldi S, Alaefour I, Unsworth G, Li X. Development of a low temperature decal transfer method for the fabrication of proton exchange membrane fuel cells. *International Journal of Hydrogen Energy* 2017;42:11813–22. doi:10.1016/j.ijhydene.2017.02.127.
- [39] Xu C. Enhanced Durability of Pt Alloy Nanoparticles Using Sulfur- Doped Graphene via Metal-Support Interactions for PEMFC Cathode Catalysis of ORR by 2017.
- [40] Sepp S, Vaarmets K, Nerut J, Tallo I, Tee E, Kurig H, et al. Enhanced stability of symmetrical polymer electrolyte membrane fuel cell single cells based on novel hierarchical microporous-mesoporous carbon supports. *Journal of Solid State Electrochemistry* 2017;21:1035–43. doi:10.1007/s10008-016-3448-4.
- [41] Shahgaldi S, Hamelin J. The effect of low platinum loading on the efficiency of PEMFC's electrocatalysts supported on TiO₂-Nb, and SnO₂-Nb: An experimental comparison between active and stable conditions. *Energy Conversion and Management* 2015;103:681–90. doi:10.1016/j.enconman.2015.06.050.

- [42] Wei Z, Su K, Sui S, He A, Du S. High performance polymer electrolyte membrane fuel cells (PEMFCs) with gradient Pt nanowire cathodes prepared by decal transfer method. *International Journal of Hydrogen Energy* 2015;40:3068–74. doi:10.1016/j.ijhydene.2015.01.009.
- [43] The US Department of Energy (DOE). Energy Efficiency and Renewable Energy http://www.eere.energy.gov/hydrogenandfuelcells/mypp/pdfs/fuel_cells.pdf and the US DRIVE Fuel Cell Technical Team Technology Roadmap (revised June 2013).
- [44] Chun JH, Park KT, Jo DH, Lee JY, Kim SG, Park SH, et al. Development of a novel hydrophobic/hydrophilic double micro porous layer for use in a cathode gas diffusion layer in PEMFC. *International Journal of Hydrogen Energy* 2011;36:8422–8. doi:10.1016/j.ijhydene.2011.04.038.
- [45] Latorrata S, Gallo Stampino P, Cristiani C, Dotelli G. Novel superhydrophobic microporous layers for enhanced performance and efficient water management in PEM fuel cells. *International Journal of Hydrogen Energy* 2014;39:5350–7. doi:10.1016/j.ijhydene.2013.12.199.
- [46] Weng FB, Hsu CY, Su MC. Experimental study of micro-porous layers for PEMFC with gradient hydrophobicity under various humidity conditions. *International Journal of Hydrogen Energy* 2011;36:13708–14. doi:10.1016/j.ijhydene.2011.07.141.

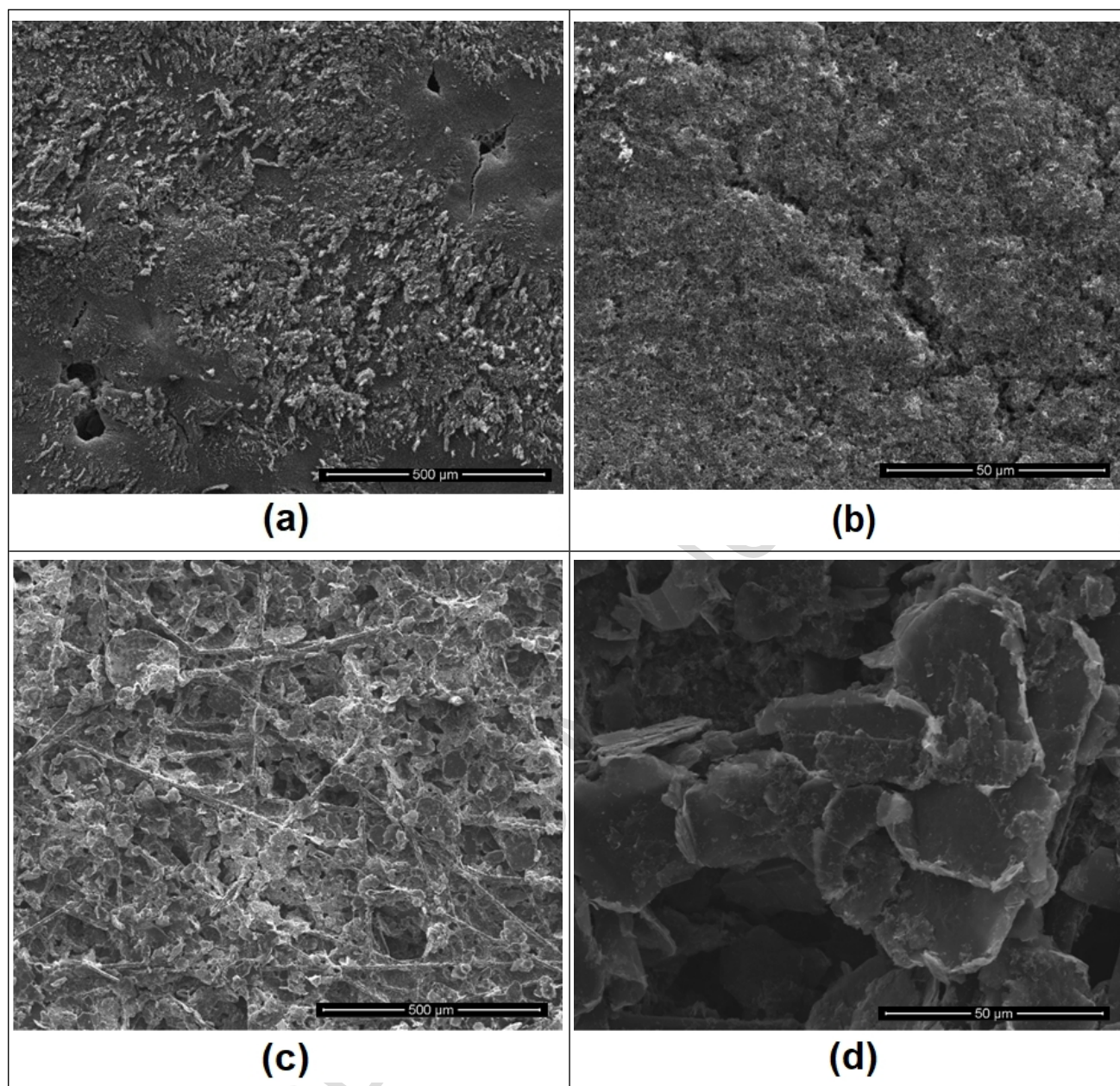


Fig. 1. Scanning electron microscopy (SEM) images of the anode and cathode gas diffusion layers (GDLs): (a-b) surface morphology of the anode GDL (commercial double-layer GDL) with the MPL surface shown; (c) surface morphology of the cathode GDL (the graphene-based MPL deposited onto the single-layer GDL); (d) arrangement of the macro-scale flake-like graphene particles on the surface of the single-layer GDL.

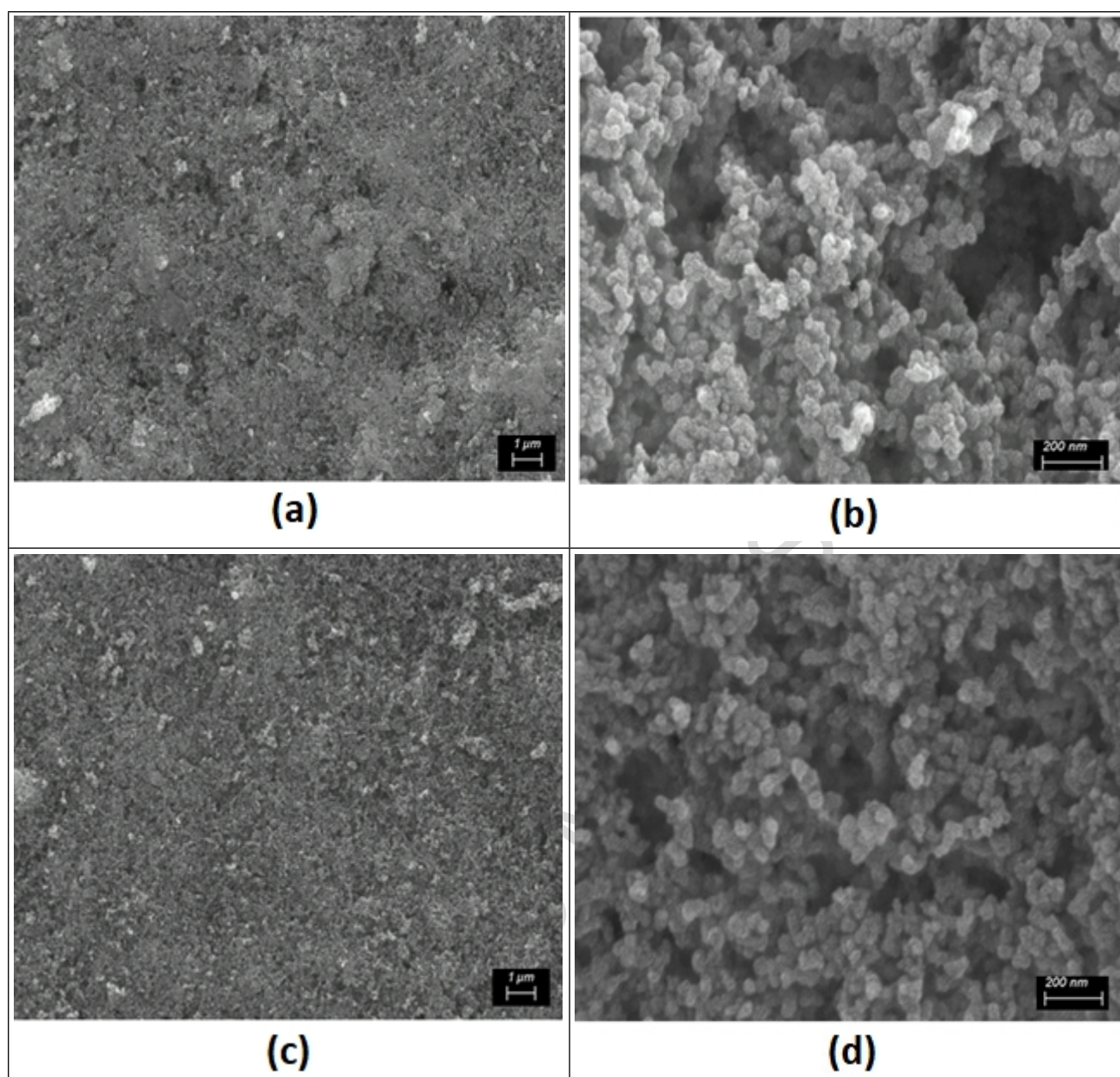


Fig. 2. Scanning electron microscopy (SEM) images of the anode and cathode catalyst layers (ACL and CCL, respectively): (a-b) surface morphology of the ACL (Pt loading: 0.10 mg/cm² and Pt/C-ionomer: 3.0/1.0); (c-d) surface morphology of the CCL (Pt loading: 0.40 mg/cm² and Pt/C-ionomer: 3.0/1.0).

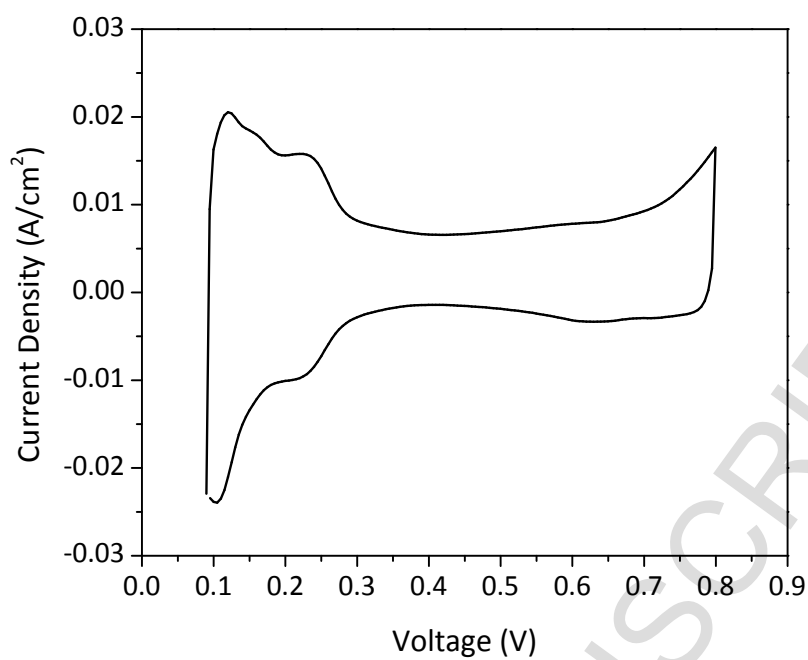
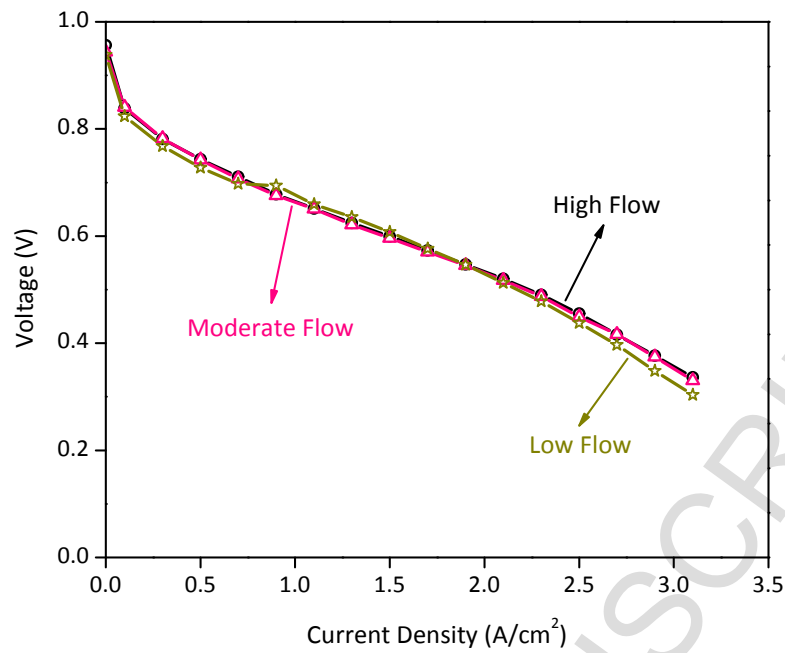
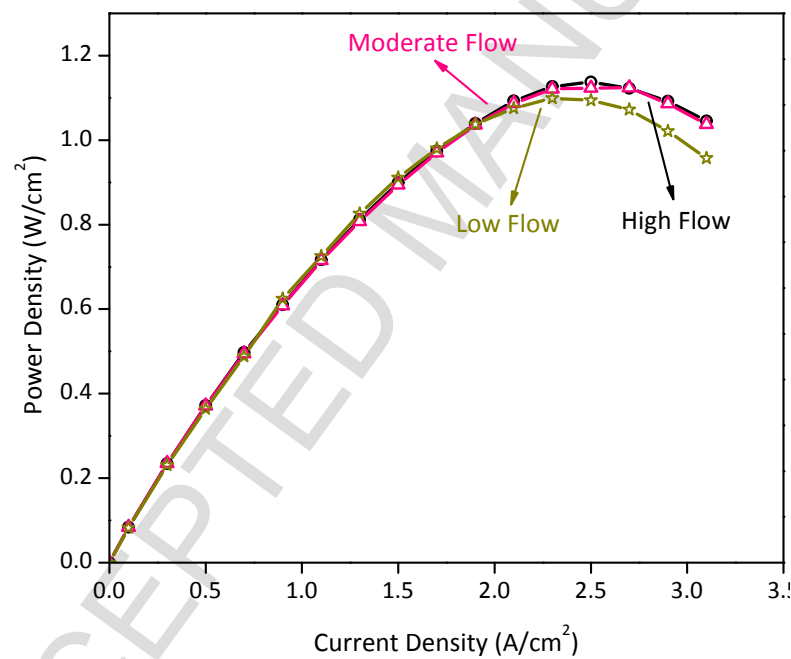


Fig. 3. Cyclic voltammograms (CVs) for the proposed membrane electrode assembly (MEA). Cell temperature: 75°C, anode and cathode back pressures: 35 kPag, anode and cathode relative humidities (RHs): 100%, and anode and cathode flow rates: 4.45 and 9.00 L/min.

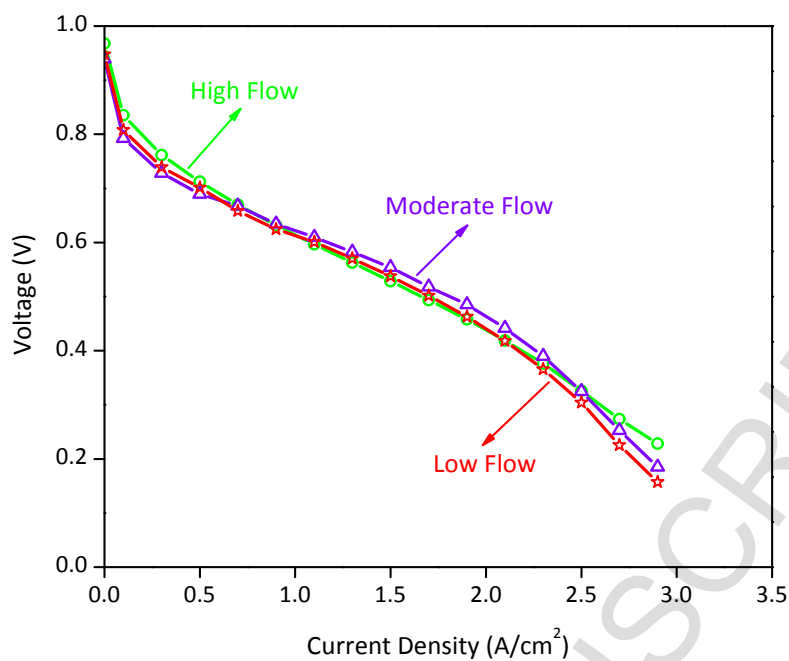


(a)

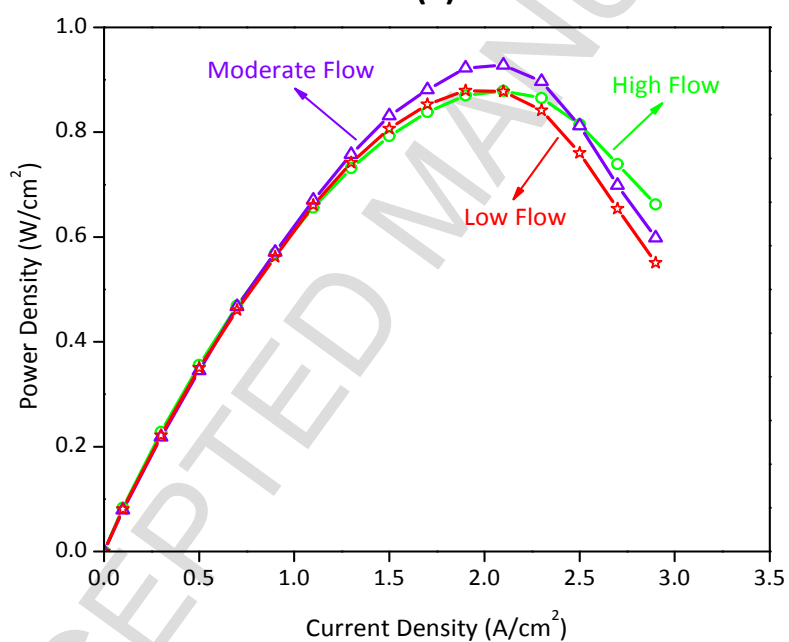


(b)

Fig. 4. (a) Polarization and (b) power curves obtained from the membrane electrode assembly (MEA) under low- (anode and cathode stoichiometries of 1.20 and 1.50), moderate- (anode and cathode stoichiometries of 1.50 and 4.00), and high-flow (anode and cathode flow rates of 4.45 and 9.00 L/min) conditions. Cell temperature: 75°C, anode and cathode back pressures: 35 kPag, anode and cathode relative humidities (RHs): 100%.



(a)



(b)

Fig. 5. (a) Polarization and (b) power curves obtained from the membrane electrode assembly (MEA) under low- (anode and cathode stoichiometries of 1.2 and 1.5), moderate- (anode and cathode stoichiometries of 1.5 and 4.0), and high-flow (anode and cathode flow rates of 4.45 and 9.00 L/min) conditions. Cell temperature: 75°C, anode and cathode back pressures: 35 kPag, anode and cathode relative humidities (RHs): 70%.

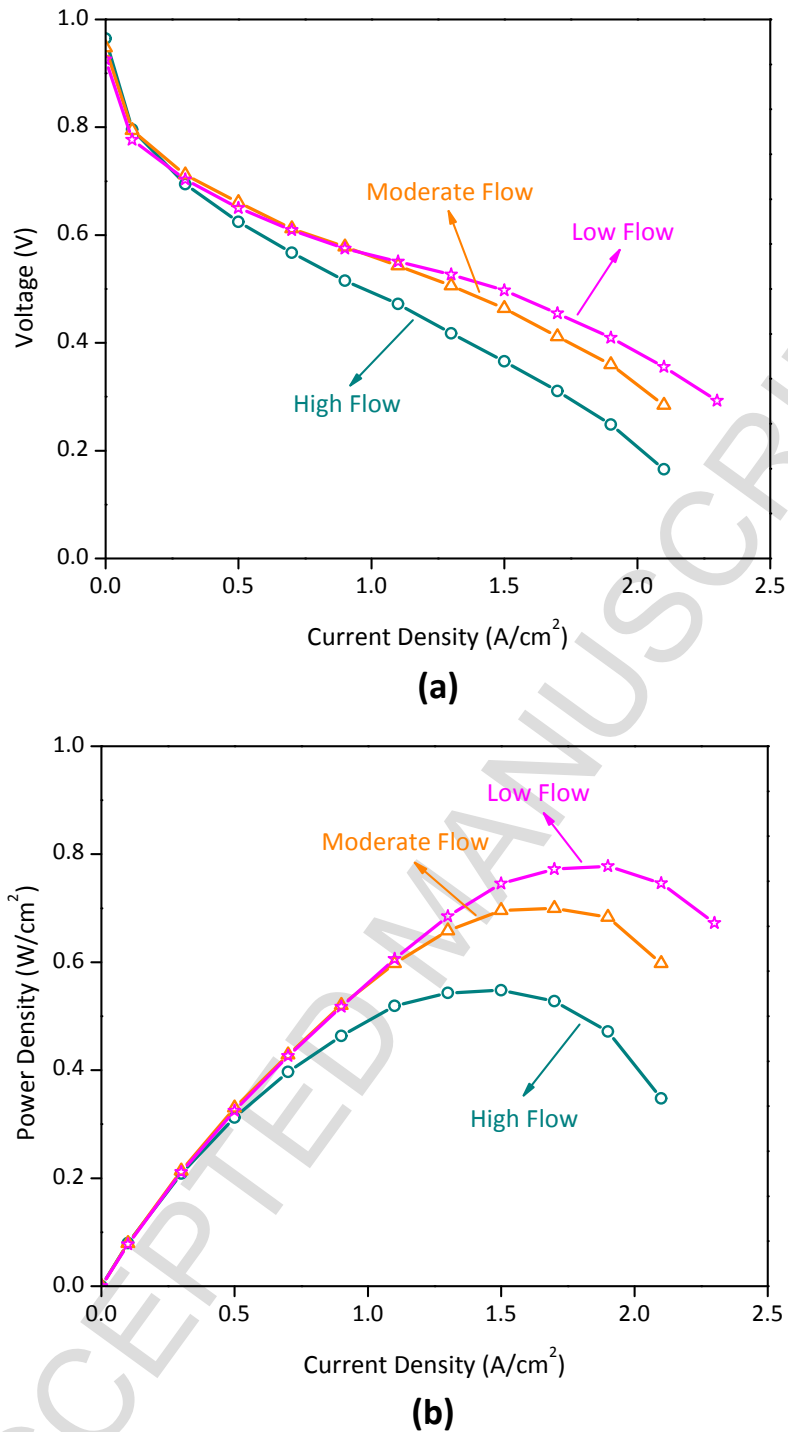


Fig. 6. (a) Polarization and (b) power curves obtained from the membrane electrode assembly (MEA) under low- (anode and cathode stoichiometries of 1.2 and 1.5), moderate- (anode and cathode stoichiometries of 1.5 and 4.0), and high-flow (anode and cathode flow rates of 4.45 and 9.00 L/min) conditions. Cell temperature: 75°C, anode and cathode back pressures: 35 kPag, anode and cathode relative humidities (RHs): 40%.

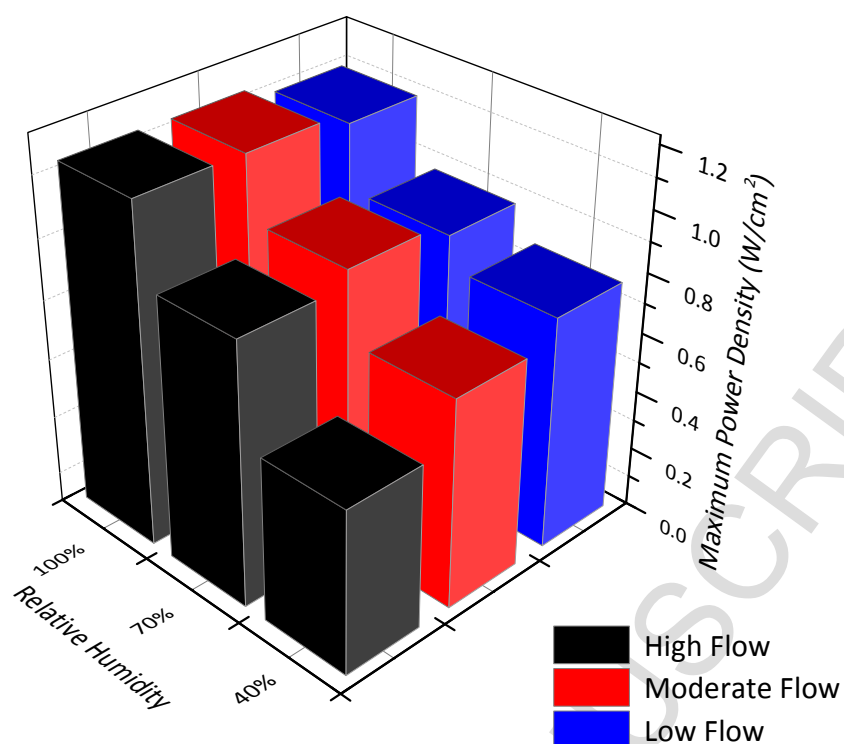


Fig. 7. Peak power densities obtained from the membrane electrode assembly under different relative humidities and flow conditions. Cell temperature: 75°C; backpressure: 35 kPag; flow conditions: anode and cathode stoichiometries of 1.2 and 1.5 (low flow); 1.5 and 4.0 (moderate flow); and 4.45 and 9.00 L/min (high flow), respectively.

Table 1. Summary of the microstructural characteristics of the single-layer gas diffusion layer (GDL), anode and cathode GDLs (meaning with MPL), and anode and cathode electrodes.

MEA component	Bulk density (g/cm ³)	Mean pore size (nm)	Total pore surface area (cm ²)	Total pore volume (cm ³)	Total porosity (%)	Ratio of local porosity total porosity		
						d ≤ 0.07 (μm)	0.07 ≤ d ≤ 5 (μm)	5 ≤ d (μm)
Single-layer GDL	0.2209	194.2	20538	0.0997	74.9	5.3%	43.2%	51.5%
Cathode GDL	0.2810	170.3	23561.43	0.1003	67.1	7.4%	54.8%	37.8%
Cathode electrode	0.3843	120.3	48520.8	0.1459	63.8	16.9%	51.8%	31.3%
Anode GDL	0.2703	118.62	45348.4	0.1345	74.3	14.4%	47.5%	38.1%
Anode electrode	0.2995	109.5	51335.6	0.1405	71.1	17.1%	46.2%	36.7%

Note: 1. Total surface area and pore volume data are calculated for two pieces of specimen.

2. Single-layer GDL refers to Avcarb EP40.

3. Cathode GDL refers to the double-layer GDL made of graphene MPL (Single-layer GDL+graphene MPL).

4. Cathode electrode refers to the cathode GDL+CCL.

5. Anode GDL refers to the commercial double-layer GDL (Avcarb GDS3250).

6. Anode electrode refers to the anode GDL+ACL.

Table 2. Summary of the physical characteristics of the porous cell components employed in the proposed membrane electrode assembly (MEA) design.

Porous cell component	MPL carbon loading (mg/cm ²)	PTFE content (%)	Thickness (μm)	Static contact angle (°)	Through-plane air permeability (m ²)
Single-layer GDL	N/A	0	181-185	144-150	(6.22-7.11) x 10 ⁻¹²
Cathode GDL	1.0	20.0	196-200	150-154	(9.17-9.64) x 10 ⁻¹⁴
Cathode electrode	N/A	N/A	208-211	156-159	(2.17-2.31) x 10 ⁻¹⁴
Anode GDL	N/A	N/A	223-227	152-156	(1.33-1.41) x 10 ⁻¹³
Anode electrode	N/A	N/A	229-232	155-158	(5.92-6.11) x 10 ⁻¹⁴

Note: 1. Single-layer GDL refers to Avcarb EP40.

2. Cathode GDL refers to the double-layer GDL made of graphene MPL (Single-layer GDL+graphene MPL).

3. Cathode electrode refers to the cathode GDL+CCL.

4. Anode GDL refers to the commercial double-layer GDL (Avcarb GDS3250).

5. Anode electrode refers to the anode GDL+ACL.